Microscopic Evidence of Upconversion-Induced Near-Infrared Light Harvest in Hybrid Perovskite Solar Cells

Mathilde Schoenauer Sebag, Zhelu Hu, Karmel de Oliveira Lima, Hengyang Xiang, Patrick Gredin, Michel Mortier, Laurent Billot, Lionel Aigouy, Zhuoying Chen

Microscopic Evidence of Upconversion-Induced Near-Infrared Light Harvest in Hybrid Perovskite Solar Cells

Mathilde Schoenauer Sebag,[†] Zhelu Hu,[†] Karmel de Oliveira Lima,[‡] Hengyang Xiang,[†] Patrick Gredin,[‡,#] Michel Mortier,[‡] Laurent Billot,[†] Lionel Aigouy,[†] and Zhuoying Chen[†,]*

[†] LPEM, ESPCI Paris, PSL Research University, Sorbonne Université, CNRS, 10 Rue Vauquelin, 75005 Paris, France

[‡] Institut de Recherche de Chimie Paris, Chimie Paris Tech, PSL Research University, CNRS, 11 Rue Pierre et Marie Curie, 75005 Paris, France

[#] Sorbonne Université, Faculté des Sciences, UFR 926, 4 place Jussieu, 75005 Paris, France

KEYWORDS: photon upconversion, upconversion solar cells, perovskite solar cells, upconversion nanoparticles, light-beam induced current

ABSTRACT. Photon upconversion represents a promising avenue to reduce the spectral mismatch losses limiting the efficiency of solar cells. Here we studied in detail the impact of inserting Yb^{3+}/Er^{3+} co-doped KY_7F_{22} upconversion nanoparticles (UCNPs) into the different interfaces of a solution-processed mixed-cation lead mixed-halide perovskite solar cell. Besides macroscopic photovoltaic characteristics, we quantify the upconversion contribution by the light-beam induced

current/fluorescence mapping technique on devices with only half of their interfaces decorated by UCNPs. Such mapping experiments offer a detailed microscopic and spectroscopic picture allowing a correlation of the electrical and optical contribution of UCNPs together with the solar cell morphology.

TEXT. Photon upconversion, a phenomenon to convert low energy photons into high energy ones, has been a fascinating topic since its discovery.[1] Over the last decades various material systems have been identified among which fluoride,[2] oxide[3] and oxysulfide[4] matrixes doped or co-doped by trivalent lanthanide ions are major examples capable to perform upconversion through a two- or multi-photon mechanism.[5] Extensive investigation has since been carried out to achieve upconversion systems in the form of nanoparticles (NPs),[6–9] facilitating their application in different fields including biomedical engineering,[10–12] optical amplification,[13] thermal sensing,[14] photodetection,[15] and solar energy harvest.[16,17] In particular, for photovoltaics, upconversion materials have been considered a promising avenue to reduce the spectral mismatch losses limiting the efficiency of solar cells.[16–18] Spectral mismatch losses, also called transmission or sub-bandgap losses, originate from the fact that photons of energies below the absorption threshold of the photovoltaic absorber cannot be absorbed and cannot contribute to the current generation in the solar cell. Such sub-bandgap losses can be quite significant: For single-junction crystalline silicon solar cells with a bandgap of 1.1 eV, sub-bandgap losses account for more than 19% of the power incident from the sun.[17] This percentage is even more elevated, reaching 39%, for solution-processed organic-inorganic hybrid perovskite halide solar cells due to their larger bandgap (e.g. about 1.5 eV for methylammonium lead iodide perovskite).[17] While low-bandgap semiconducting materials can allow an enlarged solar spectrum harvest, single-junction solar cells based on low-bandgap materials will however exhibit a reduced open-circuit voltage.[19]

Various forms of upconversion materials have therefore been applied into solar cells based on different semiconducting materials. Yb^{3+} and Er^{3+} co-doped materials represent the most widely investigated upconversion systems while other rare-earth other activators (such as Tm^{3+} and/or Ho^{3+} together with Yb^{3+}) can also be used to achieve various unconverted fluorescence in the visible spectrum.[20] They are applied in a position either before or after the illumination reaches the semiconducting absorber (termed below as "front" or "rear" side respectively). For example, a Yb^{3+} and Er^{3+} co-doped vitroceramic layer has been placed on the rear side of a GaAs solar cell capable to harvest a sub-bandgap illumination (1.39 eV) and generate a photovoltaic efficiency of 2.5%.[21] Polycrystalline 20% Er^{3+}-doped $NaYF_4$, mixed with near-infrared (NIR) transparent white oil, was adhered to the rear side of a crystalline silicon solar cell exhibiting an external quantum efficiency (EQE) close to 3.4% at 1523 nm (at 6mW).[22] On solution-processed solar cells, a front-side application of upconversion materials is the main configuration used by different works: For example, a Yb^{3+} and Er^{3+} co-doped TiO_2 layer has led to a 2.4% increase of short-circuit current in dye-sensitized solar cells.[23] Similarly, Ho^{3+}, Yb^{3+} and F^- tridoped TiO_2 NPs were applied in dye-sensitized solar cells leading to a 37% enhancement of power conversion efficiency (PCE) compared to pristine device without any upconversion layer.[24] On P3HT:PCBM organic solar cells, an upconversion quantum efficiency of 0.19% was observed under the illumination of a 975 nm laser diode (at 250 mW cm^{-2}) when both a Yb^{3+} and Er^{3+} co-doped yttrium fluoride upconversion phosphor and a NIR filter was placed in the front side of the cell.[25] On methylammonium lead iodide perovskite solar cells, by a front-side configuration, He *et al.* applied Yb^{3+} and Er^{3+} co-doped $NaYF_4$ NPs as the mesoporous scaffold directly on the compact TiO_2 layer and observed an increase of PCE from 17.8% to 18.1% upon 975 nm laser illumination (at 28 W cm^{-2}).[26] While these results are highly encouraging, the application of upconversion NPs (UCNPs)

in the front side of the solar cell (before the illumination reaches the semiconducting layer) can render the mechanistic study very complex due to the possible structural/morphological modification of the absorber materials deposited on top and the optical scattering induced by the UCNPs. In addition, unless an NIR filter was applied together with the upconversion layer, defect[27] and/or charge-transfer complex-induced[28] sub-bandgap states may also contribute to the observed photocurrents under NIR illumination leading to an over-estimation of upconversion contribution. Most above-mentioned studies are based on current-voltage characterizations, a more detailed photovoltaic-microscopic correlation characterization would be valuable to reveal the intrinsic upconversion contribution.

In this work, we present both a macroscopic and microscopic characterization of the upconversion-induced NIR light harvest in solution-processed hybrid perovskite solar cells. Uniform and well-crystalline KY_7F_{22} UCNPs with an average diameter of 183 nm co-doped by 20 mol% Yb^{3+} and 5 mol% Er^{3+} were inserted into the different interfaces of a functional solar cell based on mixed-cation lead mixed-halide perovskite $FA_{0.83}Cs_{0.17}Pb(I_{0.6}Br_{0.4})_3$ (FA = formamidinium $[HC(NH_2)_2]$). Besides the optimizations on the amount of UCNPs based on macroscopic photovoltaic characteristics, we performed detailed microscopic characterizations by the light-beam induced current (LBIC)/fluorescence mapping technique on solar cells with only half of their interface decorated by UCNPs fabricated on purpose. Such mapping experiments provided detailed microscopic and spectroscopic evidence allowing one to correlate the electrical and optical contribution of UCNPs together with the solar cell morphology.

Uniform and well-crystalline KY_7F_{22} UCNPs co-doped by 20 mol% Yb^{3+} and 5 mol% Er^{3+} were synthesized by a co-precipitation method.[29] Detailed synthesis procedure and characterization methods are described in the supporting information (SI). The nature and crystallinity of the as-

synthesized UCNPs were controlled using powder XRD. The as-recorded XRD pattern was carefully compared with that of a reference (SI Figure S1). The good agreement between both patterns and the absence of extra-diffraction lines indicated clearly that the synthesized compound was KY_7F_{22}. Moreover, the high intensity and the rather sharp profile of the diffraction peaks indicated a good crystallinity of the final product. As synthesized UCNPs were stable below about 400°C based on thermogravimetric analysis/differential thermal analysis (TGA/DTA) exhibiting a strong sharp peak at around 400°C (SI Figure S2). The XRD pattern obtained after annealing at above 400°C exhibited a different pattern composed of diffraction peaks due to KY_3F_{10} and YF_3. KY_7F_{22} is thus advantageous by comparison to the more well-known upconversion host $NaYF_4$, where cubic and hexagonal phases often co-exist but only the hexagonal ones favour efficient luminescence properties.[6] As indicated in the inset of Figure 1a, the upconversion processes in KY_7F_{22}:20% Yb^{3+}/5% Er^{3+} is believed to be similar as those in Yb^{3+}/Er^{3+} co-doped $NaYF_4$, involving the excitation of Yb^{3+} by the NIR excitation, followed by energy transfer from Yb^{3+} to Er^{3+} and the radiative decays of Er^{3+}.[30] Under 975 nm NIR excitation, three strong upconversion fluorescence emission peaks were observed at about 525 nm, 543 nm, and 655 nm corresponding to the $^2H_{11/2}\rightarrow{}^4I_{15/2}$, $^4S_{3/2}\rightarrow{}^4I_{15/2}$, and $^4F_{9/2}\rightarrow{}^4I_{15/2}$ transitions of Er^{3+}(Figure 1a). A relatively weak upconversion fluorescence at about 408 nm was also observed (not shown in Figure 1a). KY_7F_{22}:20% Yb^{3+}/5% Er^{3+} UCNPs exhibit rather long lifetimes of excited states (for example, approximately 300 μs for the $^4S_{3/2}\rightarrow{}^4I_{15/2}$ transition as shown in Figure 1b). These KY_7F_{22}:20% Yb^{3+}/5% Er^{3+} UCNPs thus possess the required optical properties to serve as good upconversion candidates for the hybrid solar cells studied in this work.

KY_7F_{22}:20% Yb^{3+}/5% Er^{3+} UCNPs were then inserted at the interface between the different stacking layers of a functional hybrid perovskite halide solar cell based on $FA_{0.83}Cs_{0.17}Pb(I_{0.6}Br_{0.4})_3$

(FA = formamidinium [$HC(NH_2)_2$]) (Figure 2). Here, a mixed-cation lead mixed-halide perovskite component was chosen due to their improved photostability compared to other prototype perovskite halides such as methylammonium lead iodide.[31] An electron transport layer (ETL)-free solar cell structure[32] was applied to decouple the influence of UCNP insertion and the experimental variation of ETL deposition. As synthesized KY_7F_{22}:Yb^{3+}/Er^{3+} UCNPs were dispersed in anhydrous isopropanol to form a NP suspension of a certain concentration (2 wt%, 5 wt%, 7 wt%, and 10 wt%). Each UCNP isopropanol solution was then deposited on top of either the fluorine doped tin oxide (FTO) or the perovskite layer by spin-coating. As indicated in Figure 2, this allows us to achieve the insertion of UCNPs either at the interfaces between FTO and the perovskite ("front-side" insertion) or between the perovskite and the hole-transport polymer layer ("rear-side" insertion). Scanning electron microscopy (SEM) characterizations, carried out after the UCNP deposition on top of the FTO (Fig. 2b and 2c) or the perovskite layer (Fig. 2e and 2f), revealed a globally uniform distribution of UCNPs on their substrates with an average particle diameter of 183 nm ± 8 nm. The use of a UCNP isopropanol suspension of a higher concentration indeed results an increase density of UCNPs decorated on FTO or perovskite. Even with a relatively dilute UCNP solution (2 wt%, Fig. 2b and 2e), the density of UCNPs on their substrates is not negligible with at least one UCNP within the perimeter of slightly less than one micron. Applying a UCNP solution of a higher concentration (7 wt%, Fig. 2c and 2f), some large UCNP clusters containing more than 10 NPs start to form. Various UCNP solution concentrations (2 wt%, 5 wt%, 7 wt%, and 10 wt%) were therefore applied to control the density of UCNPs during the optimization of UCNP/perovskite solar cell performance.

Solar cell fabrication was then completed after the deposition of UCNPs according to the device structures shown in Figure 2. The evolution of solar cell characteristics of UCNP-incorporated

$FA_{0.83}Cs_{0.17}Pb(I_{0.6}Br_{0.4})_3$ perovskite solar cells fabricated by the dispersion of UCNP isopropanol suspensions of different concentrations is shown in Figure 3. Here we aim to obtain the optimal amount of UCNPs to incorporate into such perovskite solar cells allowing a macroscopic photovoltaic characteristic enhancement before applying this optimal condition for microscopic studies. We compared solar cells fabricated from the same batch on the same day to avoid batch-to-batch device variations. By comparison to the control device without any UCNPs, both front and rear-side UCNP insertion can lead to a noticeable enhancement of short-circuit current (J_{sc}) when a UCNP solution of a 5-7 wt% concentration was applied (Fig. 3a). Specifically, about 5% of averaged J_{sc} enhancement was obtained when a 5 wt% UCNP solution was applied under the front- or rear-side NP insertion configuration. Such J_{sc} enhancement, however, starts to decrease with the use of a UCNP solution of a higher concentration (> 5 wt%). While a larger amount of UCNPs can result in a higher upconversion current contribution, the formation of large insulating[33] UCNP clusters can increase the solar cell series resistance as well as the surface roughness of the interface. These factors thus lead to the observed progressive reduction of J_{sc} when the UCNP solution concentration was beyond the optimal value (~ 5 wt%). Concerning the open-circuit voltage (V_{oc}), on both front- and rear-side insertion configurations we observed negligible effect when the UCNP concentration is small or moderate (≤ 7 wt%) and a reduction of V_{oc} when a 10 wt% UCNP concentration was applied. Such a reduction of V_{oc} can be due to the formation of large UCNP clusters at the interface which acts as charge recombination centers and/or perturbs the morphology of the perovskite or HTL layer formed on top. In terms of fill factor (FF), similar FF values as the control device were observed when the UCNP concentrations were ≤ 7 wt% for both front- and read-side configurations, suggesting minor deterioration of series and shunt resistances due to the insertion of UCNPs as long as their concentration was relatively low. At a

higher UCNP concentration (≥7 wt%), however, a reduction of FF can be observed in both device configurations, suggesting increased series resistance and recombination losses due to the formation of large insulating UCNP clusters. Overall, by comparison to the control device, about 5.7% and 7.4% of averaged PCE enhancement was observed respectively in the front- and rear-side UCNP insertion configuration when an optimal UCNP solution concentration (5 wt%) was applied. The current-voltage *J-V* and external quantum efficiency (EQE) characteristics of the best-performing solar cells, with and without UCNP insertion by the two device architectures are summarized in the SI (Figure S3, S4 and Table S1). Besides the above-mentioned ETL-free perovskite solar cells based on $FA_{0.83}Cs_{0.17}Pb(I_{0.6}Br_{0.4})_3$, with the obtained optimal UCNP solution concentration (5 wt%), we equally experimented planar $Cs_{0.05}FA_{0.79}MA_{0.16}PbI_{2.5}Br_{0.5}$ perovskite solar cells with a compact TiO_2 as the electron transport layer. Macroscopic *J-V* characteristics of these solar cells revealed similar effects of UCNP incorporation as those observed in ETL-free $FA_{0.83}Cs_{0.17}Pb(I_{0.6}Br_{0.4})_3$ perovskite solar cells (Figure S5 and Table S2). In the following discussion, we will focus our microscopic LBIC/fluorescence mapping experiments on ETL-free $FA_{0.83}Cs_{0.17}Pb(I_{0.6}Br_{0.4})_3$ perovskite solar cells due to the simplicity in device fabrication facilitating one to decouple the influence of UCNP incorporation and the experimental variation of ETL deposition.

We note that the results from the macroscopic solar cell characterization described above represent a global consequence of UCNP insertion on the perovskite solar cells where multiple effects (*e.g.* upconversion effect, impact on the electrical and structural characteristics) play together. In order to quantify the upconversion contribution, here we further performed a microscopic solar cell characterizations by the LBIC technique to correlate UCNP emission, upconversion-contributed photocurrent, together with the morphology of the solar cell under the

excitation of a NIR laser (at 975 nm). From the results described above, we observed that the rear-side UCNP insertion configuration allowed for slightly more optimized UCNP-incorporated perovskite solar cells than the front-side insertion configuration. We therefore focused on the rear-side UCNP insertion configuration to carry out the following microscopic studies. In addition, as the UCNPs were deposited after the perovskite crystallization, the structural impacts on perovskite crystallization due to the existence of UCNPs can be minimized. In order to facilitate LBIC-microstructure correlation, half of the perovskite/HTL interface was masked on purpose during the deposition of UCNPs (5 wt% solution used here) and thus creating solar cells with half of their perovskite/HTL interface decorated by UCNPs (Fig. 4a and 4b). From the gold contact side of such a solar cell, the two parts of the same device (with and without UCNPs) show different optical contrast under an optical microscope due to the increased surface roughness induced by the existence of UCNPs (Fig. 4c).

The LBIC/fluorescence mapping in this work was achieved by focusing a 975 nm NIR laser through the transparent side (FTO) of the solar cell at the perovskite/HTL interface where UCNPs were inserted for half of the device (Fig. 4a). The laser spot diameter was about 30 - 50 μm and the total power of the laser spot was about 100 mW. While the laser spot was fixed during mapping experiments, the position of the solar cell was controlled by a piezoelectric scanning stage. On each pixel, we recorded simultaneously the short-circuit current J_{sc} of the solar cell together with a fluorescence spectrum. A rectangular area (100 μm by 25 μm) containing both the parts with and without UCNPs was chosen for LBIC/fluorescence mapping experiments (indicated as the dark dashed line square in Fig. 4b). A typical LBIC and fluorescence mapping results were shown in Figure 4e, 4g, and 4h. When the laser spot mapped from the part of device without UCNPs to the part with UCNPs, we observed ~ 3-fold increase of J_{sc} which represented directly the upconversion

contribution from UCNPs excited by the 975 nm laser. It is worth to note that, during LBIC/fluorescence mapping experiments, as the laser was shrined from the FTO side (Figure 4a), if there exists any defect-induced photocurrent under NIR excitation, it should be identical for both parts of the (same) device with or without UCNPs. Therefore, the observed increase of photocurrent under NIR excitation when we mapped from the part without UCNPs to the part with UCNPs can represent well the upconversion contribution. In coherence with the J_{sc} mapping, an appearance of fluorescence of UCNPs was observed when the laser spot travelled from the part without to the part with UCNPs. These trends are clearly visible from the dashed line profile of the mapping results, plotted in Fig. 4f. The fluorescence spectrum recorded on the part with UCNP (e.g. at the point A of Figure 4e) exhibited two major fluorescence peaks located respectively between 517 nm and 560 nm (green fluorescence) and between 630 nm and 680 nm (red fluorescence). By comparison to the fluorescence spectrum recorded from stand-alone UCNPs deposited on a glass substrate (Fig. 1a), the green/red fluorescence intensity ratio recorded in LBIC/fluorescence mapping experiment is largely reduced. This is due to the fact that the fluorescence signal must travel through the perovskite layer before being detected during LBIC/fluorescence mapping. As the perovskite layer has a larger absorption coefficient at the green fluorescence wavelengths than red fluorescence ones, the fluorescence signal detected exhibited a reduced proportion of green/red fluorescence. This reduced UCNP green fluorescence observed therefore originated from the optical contribution of the UCNPs in a perovskite solar cell where upconversion fluorescence was absorbed by the perovskite layer. The above-described LBIC/fluorescence mapping experiments thus offer a detailed microscopic picture, by which one can find the electrical and optical contribution of UCNPs together in excellent agreement with the solar cell morphology (*i.e.* the parts with and without UCNPs).

In summary, in this work we studied in detail macroscopically and microscopically the impact of inserting UCNPs into a functional solar cell based on solution-processed mixed-cation lead mixed-halide perovskite $FA_{0.83}Cs_{0.17}Pb(I_{0.6}Br_{0.4})_3$. Uniform and well-crystalline Yb^{3+}/Er^{3+} co-doped KY_7F_{22} UCNPs were applied onto either the FTO/perovskite or the perovskite/HTL interface of a perovskite solar cell (the front- or rear-side configuration) while the density of UCNPs were controlled by their concentration in solution during the deposition. By comparison to the control device, about 6.1% and 6.5 % of averaged PCE enhancement were observed respectively in the front- and rear-side NP insertion configuration when an optimal UCNP solution concentration was applied. To quantify the upconversion contribution, microscopic solar cell characterizations by the LBIC/fluorescence mapping technique were carried out on devices with only half of their perovskite/HTL interface decorated by UCNPs fabricated on purpose. These mapping experiments offered a detailed microscopic picture allowing a correlation of the electrical and optical contribution of UCNPs together with the solar cell morphology: when the laser spot goes from the part of device without UCNPs to the part with UCNPs, together with the appearance of UCNP fluorescence, a ~ 3-fold increase of J_{sc} was observed attributed directly from the upconversion contribution. The reduced green/red ratio of the upconversion fluorescence spectra observed during mapping experiments were associated with the higher perovskite absorbance at the green fluorescence wavelength range. This served as a direct evidence for the optical contribution of the UCNPs in a perovskite solar cell where the upconversion fluorescence was harvested by the perovskite layer.

ASSOCIATED CONTENT

Supporting Information.

The supporting information is available free of charge on the ACS Publications website. Detailed experimental procedures and methods, XRD pattern of KY_7F_{22} NPs, TGA/DTA analyses of Yb^{3+} and Er^{3+} co-doped KY_7F_{22} NPs, the *J-V* characteristics of the best-performing planar ETL-free $FA_{0.83}Cs_{0.17}Pb(I_{0.6}Br_{0.4})_3$ solar cells with and without UCNP insertion, EQE characteristics, *J-V* characteristics of the best-performing planar $Cs_{0.05}FA_{0.79}MA_{0.16}PbI_{2.5}Br_{0.5}$ perovskite solar cells with a compact TiO_2 (with and without UCNP insertion), summary of the photovoltaic parameters from the best-performing planar ETL-free $FA_{0.83}Cs_{0.17}Pb(I_{0.6}Br_{0.4})_3$ perovskite solar cells and planar $Cs_{0.05}FA_{0.79}MA_{0.16}PbI_{2.5}Br_{0.5}$ perovskite solar cells with a compact TiO_2 as ETL, with and without Yb^{3+} and Er^{3+} co-doped KY_7F_{22} NPs inserted (PDF).

AUTHOR INFORMATION

Corresponding Author

* Email: zhuoying.chen@espci.fr

Notes

M. S. Sebag and Z. Hu contributed equally to this work.

Note added during manuscript revision. A paper by L. Qiu et al., published on 10 April 2018 in the *Applied Surface Science* **448**, 145-153 (2018), reports the incorporation of Yb^{3+} and Er^{3+} co-doped ß-NaYF4 nanoparticles in methylammonium lead iodide perovskite solar cells by a rear-side NP insertion configuration.

The authors declare no competing financial interest.

ACKNOWLEDGMENT

This work was supported in part by the UPNAN project (in the framework of IDEX with the reference of ANR-10-IDEX-0001-02 PSL*) and the PROCES project (ANR-17-CE05-0028-01). Z. Hu and H. Xiang acknowledge the Chinese Scholarship Council for their PhD scholarships.

REFERENCES

(1) Bloembergen, N. Solid State Infrared Quantum Counters. *Phys. Rev. Lett.* **1959**, *2*, 84–85.

(2) Kano, T.; Yamamoto, H.; Otomo, Y. NaLnF4 : Yb3 + , Er3 + (Ln : Y , Gd , La) : Efficient Green-Emitting Infrared-Excited Phosphors. *J. Electrochem. Soc.* **1972**, *119*, 1561–1564.

(3) Wittke, J. P.; Ladany, I.; Yocom, P. N. Y2O3 : Yb : Er-New Red-Emitting Infrared-Excited Phosphor. *J. Appl. Phys.* **1972**, *43*, 595–600.

(4) Yocom, P. N.; Wittke, J. P.; Ladany, I. Rare-Earth-Doped Oxysulfides for GaAs-Pumped Luminescent Devices. *Metall. Trans.* **1971**, *2*, 763–767.

(5) Auzel, F. Upconversion and Anti-Stokes Processes with F and D Ions in Solids. *Chem. Rev.* **2004**, *104*, 139–174.

(6) Schäfer, H.; Ptacek, P.; Eickmeier, H.; Haase, M. Synthesis of Hexagonal Yb3+,Er3+-Doped NaYF4 Nanocrystals at Low Temperature. *Adv. Funct. Mater.* **2009**, *19*, 3091–3097.

(7) Ghosh, P.; Patra, A. Tuning of Crystal Phase and Luminescence Properties of Eu3+ Doped Sodium Yttrium Fluoride Nanocrystals. *J. Phys. Chem. C* **2008**, *112*, 3223–3231.

(8) Zhao, J.; Sun, Y.; Kong, X.; Tian, L.; Wang, Y.; Tu, L.; Zhao, J.; Zhang, H. Controlled Synthesis, Formation Mechanism, and Great Enhancement of Red Upconversion Luminescence of NaYF4:Yb3+, Er3+ Nanocrystals/submicroplates at Low Doping Level.

J. Phys. Chem. B **2008**, *112*, 15666–15672.

(9) Wang, F.; Han, Y.; Lim, C. S.; Lu, Y.; Wang, J.; Xu, J.; Chen, H.; Zhang, C.; Hong, M.; Liu, X. Simultaneous Phase and Size Control of Upconversion Nanocrystals through Lanthanide Doping. *Nature* **2010**, *463*, 1061–1065.

(10) Idris, N. M.; Jayakumar, M. K. G.; Bansal, A.; Zhang, Y. Upconversion Nanoparticles as Versatile Light Nanotransducers for Photoactivation Applications. *Chem. Soc. Rev.* **2015**, *44*, 1449–1478.

(11) Sedlmeier, A.; Gorris, H. H. Surface Modification and Characterization of Photon-Upconverting Nanoparticles for Bioanalytical Applications. *Chem. Soc. Rev.* **2015**, *44*, 1526–1560.

(12) Wang, F.; Banerjee, D.; Liu, Y.; Chen, X.; Liu, X. Upconversion Nanoparticles in Biological Labeling, Imaging, and Therapy. *Analyst* **2010**, *135*, 1839.

(13) Zhang, D.; Chen, C.; Chen, C.; Ma, C.; Zhang, D.; Bo, S.; Zhen, Z. Optical Gain at 1535 Nm in LaF3: Er,Yb Nanoparticle-Doped Organic-Inorganic Hybrid Material Waveguide. *Appl. Phys. Lett.* **2007**, *91*.

(14) Aigouy, L.; Tessier, G.; Mortier, M.; Charlot, B. Scanning Thermal Imaging of Microelectronic Circuits with a Fluorescent Nanoprobe. *Appl. Phys. Lett.* **2005**, *87*, 1–3.

(15) Yan, C.; Dadvand, A.; Rosei, F.; Perepichka, D. F. Near-IR Photoresponse in New up-Converting CdSe/NaYF4:Yb,Er Nanoheterostructures. *J. Am. Chem. Soc.* **2010**, *132*, 8868–8869.

(16) van der Ende, B. M.; Aarts, L.; Meijerink, A. Lanthanide Ions as Spectral Converters for

Solar Cells. *Phys. Chem. Chem. Phys.* **2009**, *11*, 11081.

(17) Goldschmidt, J. C.; Fischer, S. Upconversion for Photovoltaics - a Review of Materials, Devices and Concepts for Performance Enhancement. *Adv. Opt. Mater.* **2015**, *3*, 510–535.

(18) de Wild, J.; Meijerink, A.; Rath, J. K.; van Sark, W. G. J. H. M.; Schropp, R. E. I. Upconverter Solar Cells: Materials and Applications. *Energy Environ. Sci.* **2011**, *4*, 4835.

(19) Kim, H. Do; Yanagawa, N.; Shimazaki, A.; Endo, M.; Wakamiya, A.; Ohkita, H.; Benten, H.; Ito, S. Origin of Open-Circuit Voltage Loss in Polymer Solar Cells and Perovskite Solar Cells. *ACS Appl. Mater. Interfaces* **2017**, *9*, 19988–19997.

(20) Gouveia-Neto, A. S.; Bueno, L. A.; da Costa, E. B.; Silva, E. A.; Ferrari, J. L.; Lima, K. O.; Gonçalves, R. R. Generation of Wide Color Gamut Visible Light in Rare-Earth Triply Doped Tantalum Oxide Crystalline Ceramic Powders. *J. Appl. Phys.* **2010**, *107*, 103539.

(21) Gibart, P.; Auzel, F.; Guillaume, J.-C.; Zahraman, K. Below Band-Gap IR Response of Substrate-Free GaAs Solar Cells Using Two-Photon Up-Conversion. *Jpn. J. Appl. Phys.* **1996**, *35*, 4401–4402.

(22) Shalav, A.; Richards, B. S.; Kramer, K.; Gudel, G. Improvements of an up-Conversion NaYF/sub 4/:Er/sup 3+/ Phosphor/silicon Solar Cell System for an Enhanced Response in the near-Infrared. In *Conference Record of the Thirty-first IEEE Photovoltaic Specialists Conference, 2005.*; IEEE, 2005; pp 114–117.

(23) Shan, G. Bin; Demopoulos, G. P. Near-Infrared Sunlight Harvesting in Dye-Sensitized Solar Cells via the Insertion of an Upconverter-TiO2 Nanocomposite Layer. *Adv. Mater.* **2010**, *22*, 4373–4377.

(24) Yu, J.; Yang, Y.; Fan, R.; Liu, D.; Wei, L.; Chen, S.; Li, L.; Yang, B.; Cao, W. Enhanced near-Infrared to Visible Upconversion Nanoparticles of Ho(3)(+)-Yb(3)(+)-F(-) Tri-Doped TiO(2) and Its Application in Dye-Sensitized Solar Cells with 37% Improvement in Power Conversion Efficiency. *Inorg Chem* **2014**, *53*, 8045–8053.

(25) Wang, H. Q.; Batentschuk, M.; Osvet, A.; Pinna, L.; Brabec, C. J. Rare-Earth Ion Doped up-Conversion Materials for Photovoltaic Applications. *Adv. Mater.* **2011**, *23*, 2675–2680.

(26) He, M.; Pang, X.; Liu, X.; Jiang, B.; He, Y.; Snaith, H.; Lin, Z. Monodisperse Dual-Functional Upconversion Nanoparticles Enabled Near-Infrared Organolead Halide Perovskite Solar Cells. *Angew. Chemie Int. Ed.* **2016**, *55*, 4280–4284.

(27) Ball, J. M.; Petrozza, A. Defects in Perovskite-Halides and Their Effects in Solar Cells. *Nat. Energy* **2016**, *1*, 16149.

(28) Ng, T. W.; Thachoth Chandran, H.; Chan, C. Y.; Lo, M. F.; Lee, C. S. Ionic Charge Transfer Complex Induced Visible Light Harvesting and Photocharge Generation in Perovskite. *ACS Appl. Mater. Interfaces* **2015**, *7*, 20280–20284.

(29) Assy, A.; Lin, H. J.; Schoenauer-Sebag, M.; Gredin, P.; Mortier, M.; Billot, L.; Chen, Z.; Aigouy, L. Nanoscale Thermometry with Fluorescent Yttrium-Based Er/Yb-Doped Fluoride Nanocrystals. *Sensors Actuators, A Phys.* **2016**, *250*, 71–77.

(30) Heer, S.; Kömpe, K.; Güdel, H. U.; Haase, M. Highly Efficient Multicolour Upconversion Emission in Transparent Colloids of Lanthanide-Doped NaYF4 Nanocrystals. *Adv. Mater.* **2004**, *16*, 2102–2105.

(31) McMeekin, D. P.; Sadoughi, G.; Rehman, W.; Eperon, G. E.; Saliba, M.; Horantner, M. T.;

Haghighirad, A.; Sakai, N.; Korte, L.; Rech, B.; Johnston, M. B.; Herz, L. M.; Snaith, H. J. A Mixed-Cation Lead Mixed-Halide Perovskite Absorber for Tandem Solar Cells. *Science (80-.).* **2016**, *351*, 151–155.

(32) Hu, Z.; Xiang, H.; Schoenauer Sebag, M.; Billot, L.; Aigouy, L.; Chen, Z. Compact Layer Free Mixed-Cation Lead Mixed-Halide Perovskite Solar Cells. *Chem. Commun.* **2018**, *54*, 2623–2626.

(33) Huang, B.; Dong, H.; Wong, K.-L.; Sun, L.-D.; Yan, C.-H. Fundamental View of Electronic Structures of β-NaYF4, β-NaGdF4, and β-NaLuF4. *J. Phys. Chem. C* **2016**, *120*, 18858–18870.

FIGURES

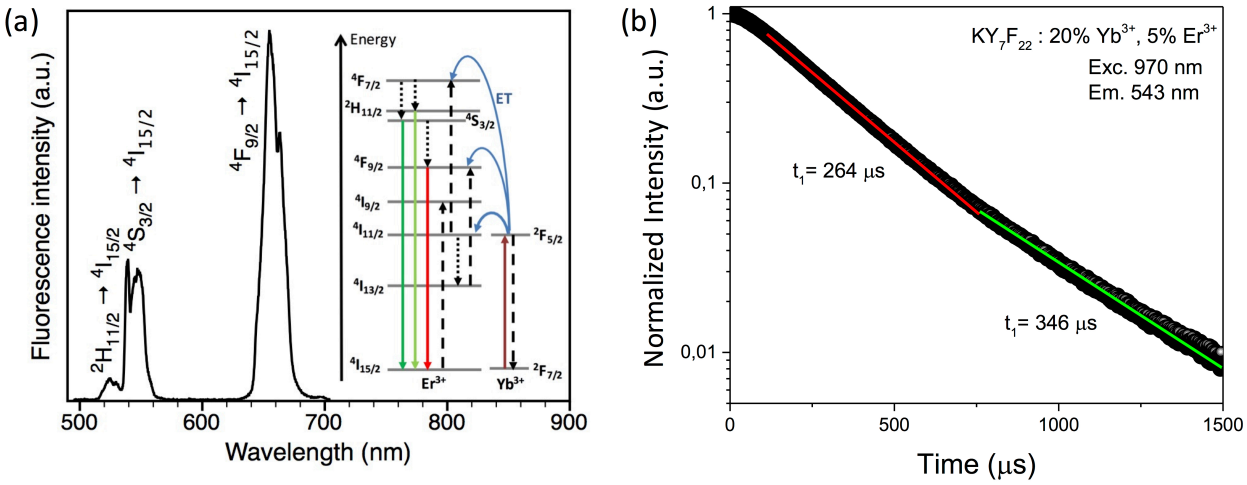

Figure 1. (a) The fluorescence spectrum of KY_7F_{22}:20% Yb^{3+}/5% Er^{3+} UCNPs under a NIR laser excitation (laser peak wavelength = 975 nm). The corresponding energy transitions are shown in the inset of the figure. (b) The fluorescence decay curve of the $^4S_{3/2} \rightarrow {}^4I_{15/2}$ transition (measured

at 543 nm) of KY_7F_{22}:20% Yb^{3+}/5% Er^{3+} UCNPs under a 970 nm NIR laser excitation. The red and the green curves represent the two single exponential fits (at short time and long time) of the experimental data together with the decay time constant.

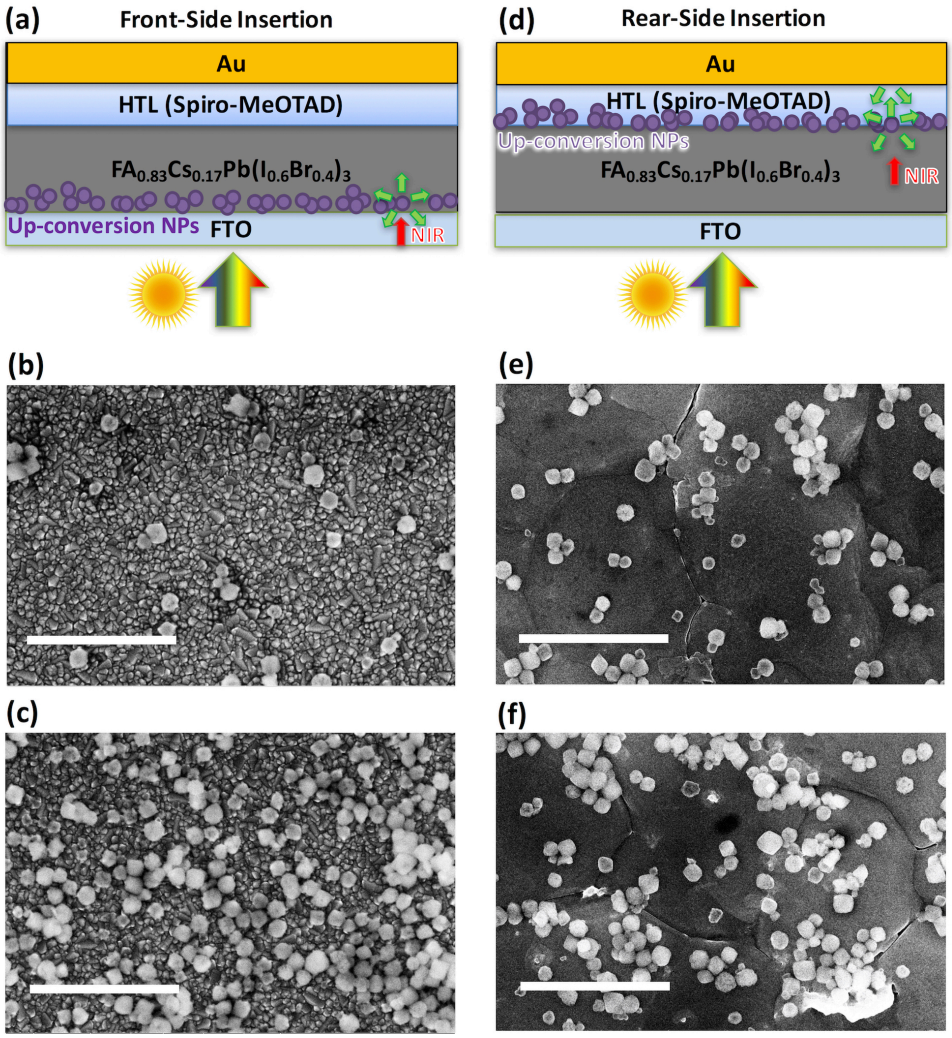

Figure 2. (a) and (d) Schematics displaying the solar cell architectures and the interface where UCNPs were deposited. HTL: hole-transport polymer layer. (b) and (c) SEM characterizations of

UCNPs deposited from a 2 wt% (b, e) and 7 wt% (c, f) isopropanol suspension on FTO (b, c) and on a $FA_{0.83}Cs_{0.17}Pb(I_{0.6}Br_{0.4})_3$ perovskite layer (e, f). Scale bar = 2 µm.

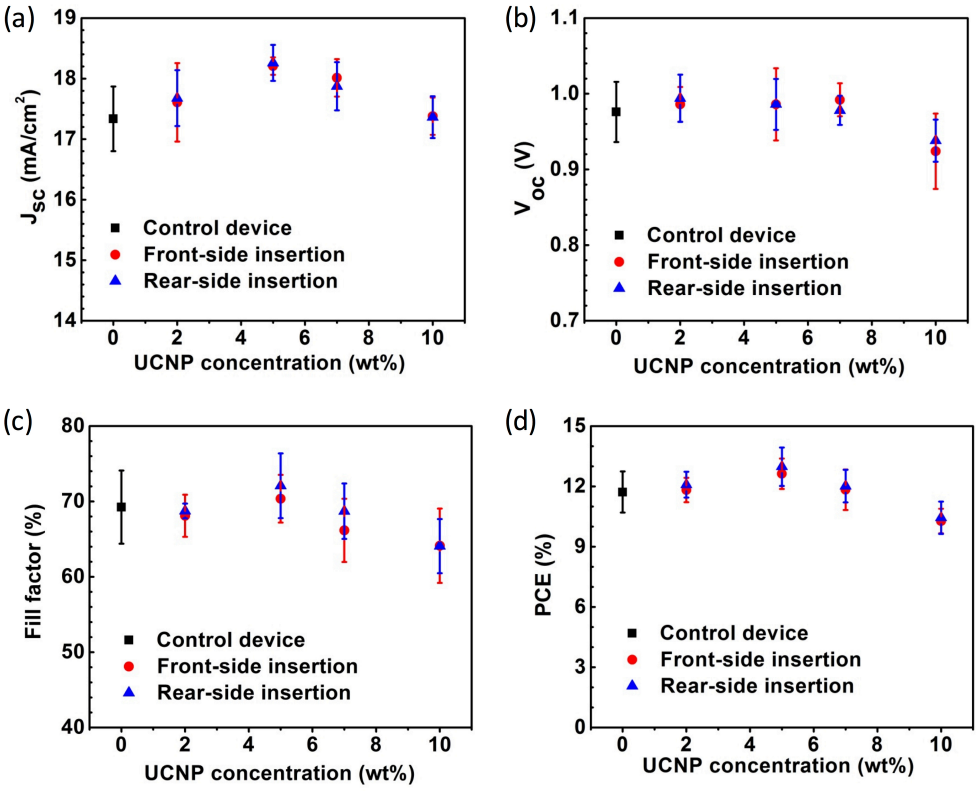

Figure 3. The evolution of (a) J_{sc}, (b) V_{oc}, (c) fill factor, and (d) PCE of UCNP-incorporated $FA_{0.83}Cs_{0.17}Pb(I_{0.6}Br_{0.4})_3$ perovskite solar cells by UCNP isopropanol suspensions of different concentrations. Device characteristics were measured under simulated AM1.5G 1-sun illumination (100 mW cm^{-2}) on solar cells fabricated from the same batch on the same day. Each error bar represented the one standard deviation based on the results from at least 5 identical devices. The control devices (0 wt% UCNPs) represent the solar cells without any UCNP incorporation. The front-side and rear-side insertion refer to the two device architectures shown in Fig. 2.

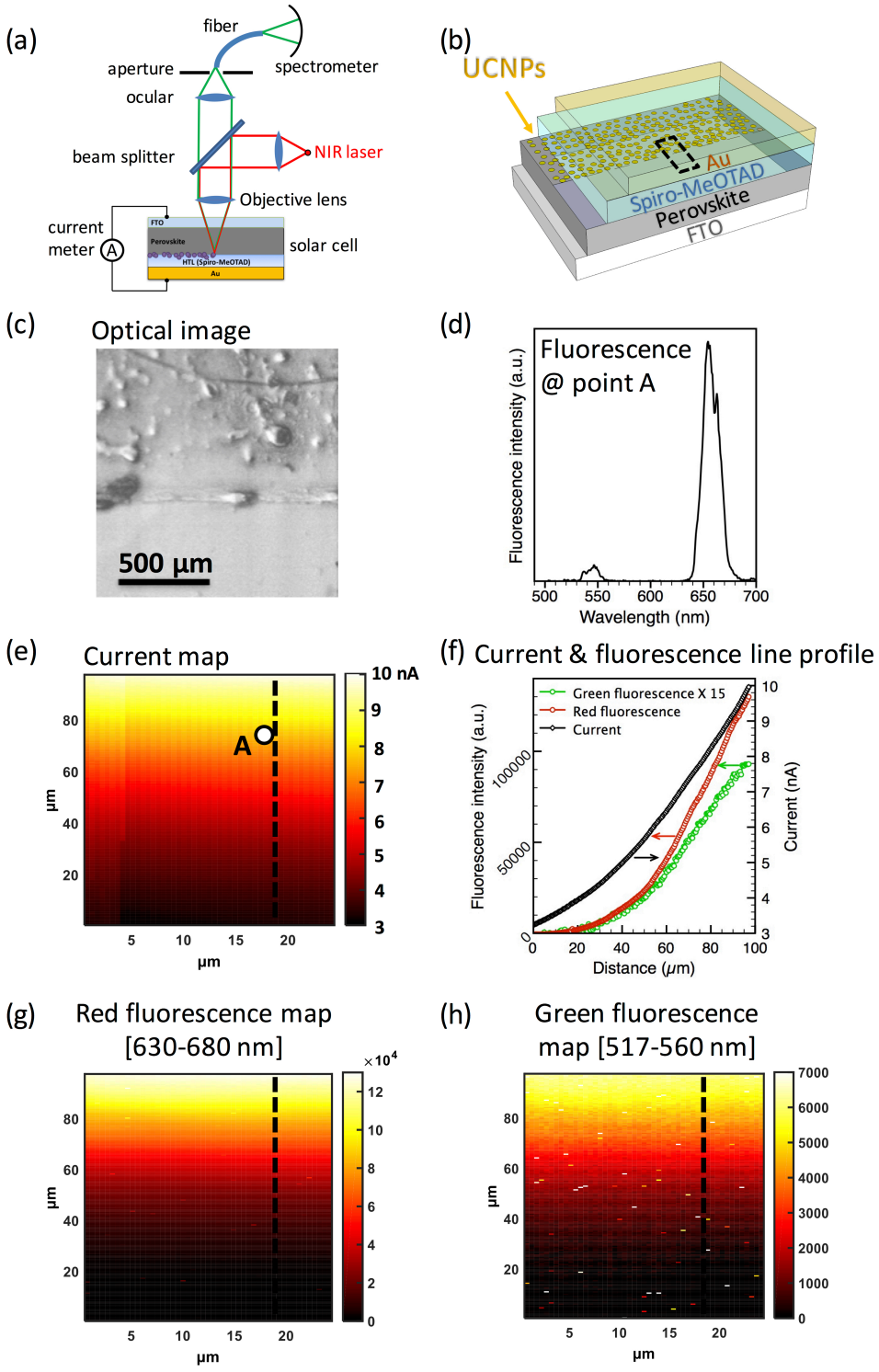

Figure 4. (a) Schematic of the LBIC/fluorescence mapping experimental set-up and the cross-sectional schematic of the UCNP-incorporated solar cell used in this work. The NIR laser (975 nm) was focused at the perovskite/HTL interface through the FTO side. (b) Schematic (not to

scale) of the UCNP-incorporated perovskite solar cell structure where half of the perovskite/HTL interface was decorated by UCNPs. The dark dashed square represents the device area where LBIC/fluorescence mapping was carried out. (c) Optical image of the top-view (imaged from the gold electrode side) of the UCNP-incorporated perovskite solar cell. The interface between the part with and without UCNPs is clearly visible. (d) The upconversion fluorescence spectrum recorded during the LBIC mapping at the point A (labelled in (e)). (e) Short-circuit current J_{sc} mapping under the excitation of a 975 nm NIR laser. (f) J_{sc} and fluorescence line profile of the dashed line shown in (e), (g) and (h). (g) and (h) The red and green fluorescence mapping recorded simultaneously during LBIC mapping. Each pixel represents the fluorescence signal integrated between 630 nm and 680 nm for red fluorescence (g) and between 517 nm and 560 nm for green fluorescence (h).

Table of Contents (TOC) Graphics